

# Emulation of Gas-Liquid Flow in Packed Beds for Offshore Floating Applications Using a Swell Simulation Hexapod

Gnouyaro P. Assima, Amir Motamed-Dashliborun, and Faïçal Larachi  
Dept. of Chemical Engineering, Laval University, Québec QC G1V 0A6, Canada

DOI 10.1002/aic.14816

Published online April 13, 2015 in Wiley Online Library (wileyonlinelibrary.com)

*A laboratory-scale packed column was positioned on a six degree of freedom swell simulation hexapod to emulate the hydrodynamics of packed bed scrubbers/reactors onboard offshore floating systems. The bed was instrumented with wire mesh capacitance sensors to measure liquid saturation and velocity fields, flow regime transition, liquid maldistribution, and tracer radial and axial dispersion patterns while robot was subject to sinusoidal translation (sway, heave) and rotation (roll, roll + pitch, yaw) motions at different frequencies. Three metrics were defined to analyze the deviations induced by the various column motions, namely, coefficient of variation and degree of uniformity for liquid saturation fluctuating fields, and effective Péclet number. Nontilting oscillations led to frequency-independent maldistribution while tilting motions induced swirl/zigzag secondary circulation and prompted nonuniform maldistribution oscillations that deteriorated with decreasing frequencies. Regardless of excited degree of freedom, a qualitative loss of plug-flow character was observed compared with static vertical beds which worsened as frequencies decreased. © 2015 American Institute of Chemical Engineers AIChE J, 61: 2354–2367, 2015*

*Keywords: swell simulator, floating production storage offloading units, offshore treatment, embarked packed bed, flow regime, liquid maldistribution, tracer dispersion*

## Introduction

It is the prevalence of the belief that the major conventional land-based fossil fuel reserves have, by and large, been discovered or are being intensively tapped that future discoveries are gradually endeavored to uncover and secure supplies from new hydrocarbon reserves especially in offshore areas.<sup>1</sup> Consequently, the development of offshore oil and gas fields has been increasingly moving toward deeper water and areas far off continental shores.<sup>2,3</sup> Remoteness of oil and gas production sites undoubtedly entails capital cost races for the offshore infrastructure to be as competitive as its well-established onshore sister.<sup>4</sup> The conventional offshore platforms most frequently built for oil/gas fields exploitation in deep seas or far offshore comprise deep draft semisubmersible, semisubmersible rigs, extendable draft or tensioned leg platforms, and single-point anchor reservoir.<sup>1,5</sup> Yet, pressed by ever changing constraints, the offshore industry has been the witness over the recent past of a technology shift that is markedly reshaping the configuration of the offshore fleet. At present, floating production storage and offloading (FPSO) units are becoming the offshore structures *par excellence* for they allow integration on the same floating systems of extraction, production, and storage operations unequalled by the other existing systems.<sup>6,7</sup> FPSO units are

especially adapted for remote oil and gas fields, small and large alike, for which the hyphenation to onshore terminals via seabed pipeline infrastructures ceases to be cost-effective.<sup>1</sup> Furthermore, when tapped wells do not justify installation of stationary platforms such as in the case of short-lived or rapidly depleting reservoirs, FPSO units offer an obvious flexibility over fixed platforms. In addition, when operating in unfriendly areas with records of high-risk cyclone or iceberg episodes, FPSO units are able to momentarily release mooring and clear off to safer waters.<sup>1</sup> Hence, despite the inconvenience of intermittent production, the mobility of FPSO units appears to offset the extra cost of reinforcing or over-designing fixed platforms. FPSO units allow the hydrocarbons to be treated and refined in the vicinity of the extraction location by means of onboard scrubbers or reactors akin to those ordinarily in service in conventional above-ground plants.<sup>8</sup> Therefore, harnessing the operation of such vessels onboard floating systems requires implementation of efficient corrective measures to counter or to anticipate any performance deviation with respect to the well-trodden land-based treatment units. More specifically, experimental and theoretical studies regarding the effect of floating vessel motions on the hydrodynamic behavior of multiphase flows in porous media within embarked packed bed systems are scarce to say the least. Currently, the main endeavors in industry focus on the design of apposite distributors and/or on the selection of packings to curb the dynamic fluid maldistribution that results from the swell-dynamics convoluted ship displacements (translation and rotation velocity, acceleration, and amplitudes) and their repercussions on the embarked packed beds themselves.<sup>9,10</sup>

Additional Supporting Information may be found in the online version of this article.

Correspondence concerning this article should be addressed to F. Larachi at faical.larachi@gch.ulaval.ca

In an approach mainly privileged by applied and industrial research laboratories, developments and innovation concerned the design of adapted distributors to ensure hydraulic charge regardless of wave conditions.<sup>9,10</sup> Recently, Institut français du pétrole (IFP) developed a distributor tray partitioned into compartments each comprising functionalities for passing gas via chimneys and liquid via perforations thus allowing an enhanced liquid repartition even under rolling conditions (angle  $\pm 5^\circ$ , period 10–20 s).<sup>11</sup> Maldistribution sensitivity and susceptibility in columns subject to horizontal accelerations and tilt were also examined in terms of flow correction or aggravation depending on the type of internals used, that is, random packing, structured packing, and trays.<sup>12</sup> To tackle phase maldistribution inside the columns, cross-corrugated packing comprising a stack of vertical corrugated strips with their corrugations alternately inclined in opposite directions was also developed to achieve an even wetting of the packing over the entire cross-section of distillation columns embarked on offshore oil platform or barge oscillating typically between  $5^\circ$  and  $10^\circ$ .<sup>13</sup>

A parallel path to the design of *ad hoc* distributors was pursued by other investigators whose interest focused on describing the hydrodynamics inside static inclined beds which were implicitly hypothesized to be limiting postures on ships when these are subject to very slow tilting motions.<sup>14–20</sup> Atta et al.<sup>14</sup> and Schubert et al.<sup>15</sup> were the first to describe experimentally and through numerical simulations the hydrodynamics in inclined trickle beds. The dependence of segregation in two-phase gas-liquid descending flows and tilt angle was investigated using electrical capacitance tomography. Significant alterations in flow behavior such as phase stratification and reduction in liquid saturation were observed with the decrease of tilt angle. These studies also revealed qualitative changes in pulse flow regime characteristics such as pulse frequency and propagation velocity as compared with their analogs as they manifest in vertical trickle beds. More recently, the hydrodynamics of two-phase gas-liquid ascending flows in inclined packed beds was studied.<sup>16</sup> Segregation between gas and liquid was observed as in inclined trickle beds and was monitored through the change with bed tilt angle of the inception of transition from the bubble flow regime to the segregated flow regime. The effect of inclination on flow regimes and recirculation patterns in gas-solid and liquid-solid inclined fluidized beds was also investigated by a few researchers. Flow regimes and transition thereof were characterized for air fluidized beds inclined between  $45^\circ$  and  $90^\circ$  and the inventory of which consisted of different types of powders.<sup>15</sup> The major shortcoming of bed inclination whereby the upper wall was identified as the region of high gas velocity that prematurely prompted localized transition to bubbling regime.<sup>18–20</sup>

Besides experimental studies, theoretical investigations have also been attempted to develop multiphase fluid dynamic models to capture the physics of local flow distribution inside packed beds. Approaches such as the relative permeability, slit, and double-slit models are the most commonly used to describe the hydrodynamic interactions in stationary vertical packed beds subject to gas-liquid cocurrent downflow.<sup>21–25</sup> Recently, Atta et al.<sup>14</sup> implemented the relative permeability model in an Eulerian computational fluid dynamics (CFD) framework to simulate the hydrodynamics in stationary tilted trickle beds. Predictions from numerical simulations were found to deviate notably from

experimentally measured liquid holdup distributions emphasizing the need for drag force closure formulations more in adequacy with the stratified flow emerging in inclined packed beds. In case of nonstationary instances, column movements have to be accounted for in the simulations. The common inertial reference-frame-based CFD models should be transformed to moving reference frame to capture the vessel emulated sea motions. Recently, Zhao et al.<sup>26</sup> established a three-dimensional (3-D) CFD-discrete element method model for simulation of a circulating fluidized bed subject to rolling motion in which the time-dependent acceleration terms were included as additional body force terms in the phasic momentum balance equations.

To the best of our knowledge, studies emulating reactor/contacter motion with relevance to marine use contented with inquiring into the effect of rolling while hitherto disregarding coupled or single effects stemming from other ship degrees of freedom, that is, surge, sway and heave (translations), and pitch and yaw (rotations). This motion was emulated by means of the crank mechanism on a rolling assembly with numerous investigations dating back to the 1980s.<sup>27–29</sup> The most recent ones were concerned with marine applications of circulating fluidized beds for sulfur removal and waste heat recovery where the effects of rolling were measured in terms of gas-solid flow and heat transfer.<sup>26,30,31</sup> The break in axisymmetry of the flow fields due to gravity, as reported in the aforementioned studies on static inclined configuration, prevailed also under rolling with an added complexity of the flow pattern due to the riser periodic rocking, for example, pressure drop increase with increased solids holdup at riser's bottom, heat-transfer augmentation along the walls<sup>29</sup> and its reduction inside the bed.<sup>32</sup>

Despite a growing significance in the area of FPSO applications, investigations focusing on the two-phase flow dynamics in floating packed beds remain, as far as open literature is concerned, an uncharted territory. Besides roll motion, floating vessels feature five other degrees of freedom which are so far fully disregarded. To provide a more comprehensive understanding into the effect of sea motion on the performances of floating production systems, this study aims at examining experimentally two special aspects, namely, liquid maldistribution and tracer liquid dispersion, in a laboratory-scale packed bed with cocurrent descending gas-liquid flow embarked on a hexapod ship motion simulator and submitted to a variety of motion regimes. Three wire mesh capacitance sensors (WMCS) intercalated at various heights along the packed bed were used to measure the local instantaneous liquid saturation and velocity. The rotational and translational degrees of freedom were implemented either one at a time or in binary combinations to allow data interpretation from the wire mesh sensors of the related bed hydrodynamics. Phase segregation and flow patterns were interpreted through monitoring a flow uniformity index while liquid dispersion was deciphered in terms of radial and axial dispersion. The instantaneous hydrodynamic behavior of the moving packed bed was also discussed in light of its limiting postures corresponding to static vertical and static inclined configurations.

## Experimental

The experimental setup shown in Figure 1 consists of transparent 5.7 cm ID Plexiglas modules (1) assembled up to

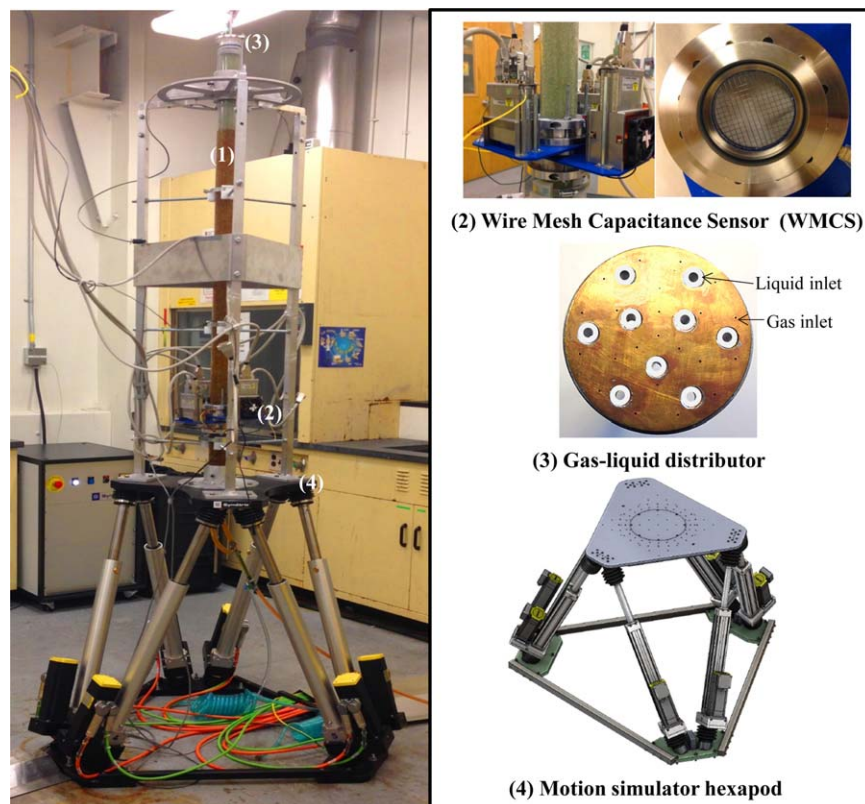


**Figure 1.** Layout and components of the hexapod/wire mesh sensor/packed bed assembly: (1) packed bed (Plexiglas column), (2) WMCS, (3) gas-liquid distributor, and (4) ship motion simulator (hexapod).

[Color figure can be viewed in the online issue, which is available at [wileyonlinelibrary.com](http://wileyonlinelibrary.com).]

a nominal height of 170 cm around flanged WMCS (2) — designed by the Institute of Fluid Dynamics, Helmholtz Zentrum Dresden, Germany—which permit measurements of local liquid saturation and velocity. The column was carefully packed in a stepwise manner<sup>33</sup> up to a height of 160 cm with 1.2 mm glass beads resulting in a bed porosity of about 0.40. To prevent displacements of the glass beads with respect to the column referential either during motion or while the bed is slanted, the packing was tightly immobilized between an uppermost gas-liquid distributor (3) and lowermost stainless steel retention grids. The distributor consisted of 22 needle orifices (ca. 0.4 mm in diameter) for gas supply and 9 capillaries (1 mm in diameter) for liquid feed (Figure 1). Experiments were performed using air and kerosene concurrent downflow at room temperature and atmospheric pressure. The liquid physical properties are summarized in Table 1. Prior to starting the experiments, the

packed bed was systematically flooded during 20 min, and then drained before to be operated for 1 h in the pulse flow regime to ensure full bed prewetting according to the established protocols.<sup>34,35</sup>

### Hexapod platform

The modular column was tightly immobilized on a NOTUS hexapod platform (4) (Symétrie, Nîmes, France) which provided accurate control over the six degrees of freedom to emulate the motion of floating vessels: three translations (surge, along X direction; sway, along Y direction; heave, along Z direction) and three rotations (roll, around X axis; pitch, around Y axis; yaw, around Z axis) as shown Figure 2a. One-at-a-time degree of freedom excitations, that is, sway, heave, roll, and yaw motions, in addition to superimposed out-of-phase roll and pitch rotations were programmed for this hydrodynamic study. As normal operation requires vertically erected columns, enabling one-at-a-time surge (respectively, roll) motion on the hexapod leads to an equivalent disposition as sway (respectively, pitch) motion. Schematic illustrations of the one-at-a-time motions are displayed in Figure 2b. Sinusoidal excitations with three frequencies, namely, 0.05, 0.1, and 0.2 Hz were tested to cover a frequency range typical of wind-generated fully developed sea conditions.<sup>36</sup> The hexapod programmed motion parameters are given in Table 2 while representative video animations of the packed column subject to these selected motions are displayed in the Supporting Information (Appendix A). Angular and translation amplitudes up to 15° and 250 mm, respectively, were covered. For combined roll and pitch, the roll and pitch paths were performed simultaneously with a

**Table 1.** Physical Properties of Kerosene and Composition of Organic Tracer Solution

		Property
Kerosene	Density (kg/m <sup>3</sup> )	789
	Viscosity (mPa.s)	1.05
	Surface tension (mN/m)	25.3
SR1795	Component	Wt %
	Toluene	10–20
	Dodecylbenzene sulfonic acid	2–8
	Kerosene	60–70
	Naphtha solvent	2–7
	Polysulfone	2–7
	Amine polymer	2–8

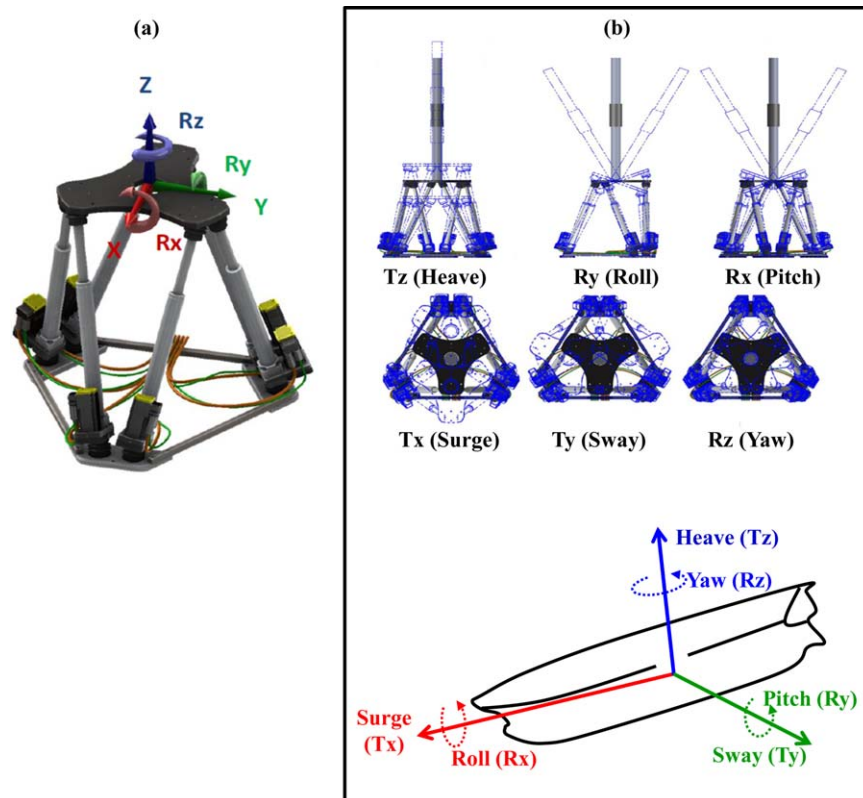


**Figure 2. Ship motion simulator apparatus (a) hexapod platform and its six degree of freedom motion and (b) translational and rotational hexapod and ship motions.**

[Color figure can be viewed in the online issue, which is available at [wileyonlinelibrary.com](http://wileyonlinelibrary.com).]

90° phase lag (Table 2). In addition, static vertical (0°) as well as static inclined (5°, 10°, and 15°) columns were also studied to fully compare offshore vs. conventional onshore configurations. After the start of each motion sequence, a minimum of 30-min wait time was maintained prior to data collection to ensure the start-up transients had died out at the expense of the cruise-regime transients within the packed bed.

#### Wire mesh sensor

Flange-connectible modules of twin or single WMCS were intercalated along the packed bed at prescribed elevations (Figure 3). The latter WMCS enabled crosswise liquid saturation cartographies at given bed height, whereas in the twin sensor arrangement, local velocity events were accessible by cross-correlation of signal time series from pixel pairs facing above each other with a vertical separation equal 12 mm. Each wire mesh sensor consisted of two orthogonally arranged (upstream and downstream) planes, 1.5 mm afar, of 16 parallel stainless steel wires (0.4 mm diameter). The upstream and downstream wire planes were, respectively, run in transmission and reception modes. Such

arrangement of planes resulted in 256 reading points, among which 188 points fell inside the column circular cross-section. Adjacent reading points defined an in-plane wire separation square of  $3.57 \times 3.57 \text{ mm}^2$  (one pixel) with the exception of the pixels overlapping with the column wall for which only their areal fractions inscribed within the vessel were taken into account.

Exhaustive information on the WMCS functionalities and data processing can be found elsewhere.<sup>33,37</sup> Summarily, the technique gives access to a local multiphase mixture permittivity measurement at each touchless nodal (cross-point) voxel where each pair of normally aligned transmitting and receiving wires meet (Figure 1). To permit signal disambiguation of the excited nodal voxels, the sensor electronics briefly excites but one transmitting wire during a few microseconds with a high-frequency (ca. 5 MHz) AC voltage while keeping all the other transmitting wires idle at ground potential. The resulting AC currents in the receiving wires of the downstream plane are detected in parallel by means of amplifiers, logarithmic stage, and A/D converters.<sup>38</sup> Sweeping sequentially each individual transmitter wire allows signal acquisition of all touchless cross-points. A sampling

**Table 2. Tested Hexapod Motions and Related Characteristics**

Motion	Frequency (Hz)	Phase Lag (°)	Amplitude (mm or °)
Roll (Rx)	0.05/0.1/0.2	0	15°
Roll + pitch (Rx + Ry)	0.05/0.1/0.2	90° for Rx and 0 for Ry	15° and 15°
Yaw (Rz)	0.05/0.1/0.2	0	15°
Heave (Tz)	0.05/0.1/0.2	0	200
Sway (Ty)	0.05/0.1/0.2	0	250

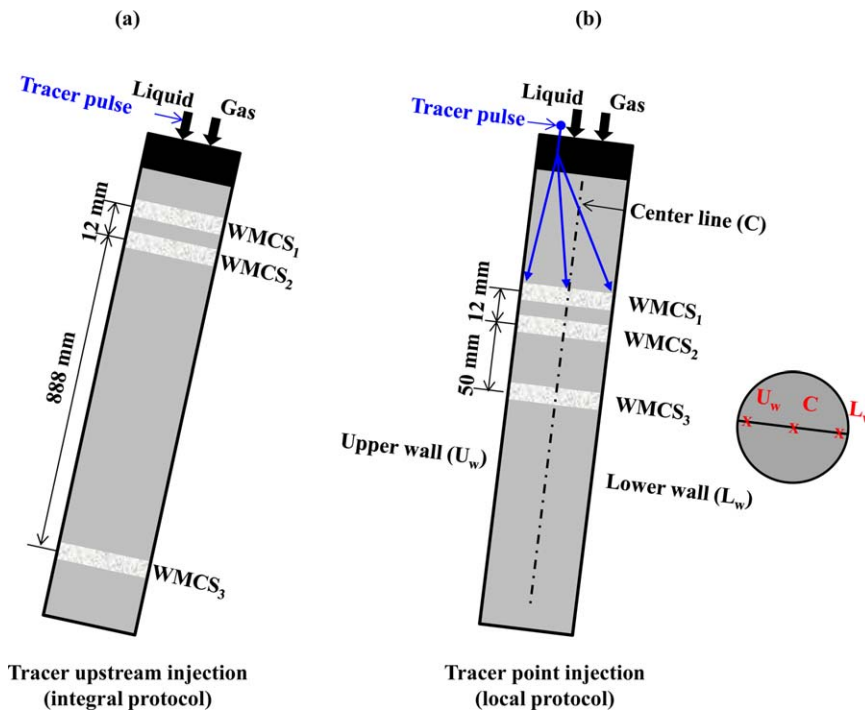


**Figure 3. Arrangements for (a) integral and (b) local tracer injections and corresponding positioning of WMCS.**

[Color figure can be viewed in the online issue, which is available at [wileyonlinelibrary.com](http://wileyonlinelibrary.com).]

frequency of 100 Hz was found enough to capture the entire frequency pass-band (<50 Hz Nyquist frequency) of the hydrodynamic phenomena of interest.

The capacitance sensor signal was converted in time and spatial quantitative information through a calibration/reconstruction procedure using the so-called two-point calibration.<sup>38</sup> Hence, the data files acquired with the limiting cases of flooded and drained columns were assigned to bed states of 100% (upper-level reference) and 0% (lower-level reference) liquid fraction, respectively. The calibration data were thereafter used for determining the dynamic liquid saturation,  $\beta$ . This latter was defined as the liquid quantity held within a given pixel divided by the pixel area and bed porosity. It is worthy of notice that the resulting liquid saturation is the contribution that exceeds the residual (or static) liquid saturation as this latter corresponds to the lower-level reference in the calibration procedure. Moreover, the pixel-affixed liquid saturation being volumetric variable is to be associated *stricto sensu* to the corresponding voxel the thickness of which is given by the 1.5 mm interplane distance between wire planes. Finally, independent drainage tests performed under the various motion modalities led, irrespective to the imposed frequency, to static liquid holdup identical to that determined in the case of static vertical column configuration.

### Tracer tests

To characterize back-mixing in the liquid flow, a kerosene-based conductivity improver (SR 1795, Dorf Ketal Chemicals LLC) was used as an electrolyte tracer<sup>39</sup> to study liquid radial and axial dispersions. The SR 1795 chemical composition is summarized in Table 1. To ensure that the injected additive will representatively trace the kerosene paths, tracer/kerosene solutions were prepared by matching as closely as possible kerosene properties. Typically, a bleed of SR 1795 (11 mL/min) was briefly injected for 5 s within

the kerosene stream. Two types of tracer injection were tested to capture both integral and local liquid mixing in the various packed bed solicitations. In the first type of injection, integral liquid mixing was assessed by means of tracer upstream injections (Figure 3a) and detection using three WMCS: two located 40 and 41.2 cm from the inlet and one mounted 30 cm from the outlet. For the local tracer injection, a stainless steel capillary tube (1 mm OD) was inserted from the top of the packed bed until its tip was right above WMCS<sub>1</sub>. This sensor was placed 60 cm from the bed entrance while the second and third WMCS followed 1.2 and 6.2 cm downstream, respectively (Figure 3b). The injection point was successively positioned on the column centerline and at two diametrically opposite upper and lower positions as sketched in Figure 3b. These selected locations, thought of as a kind of spatial Dirac-type, enabled elucidating the dynamics of liquid flow such as in the gas-rich and liquid-rich zones of inclination-induced stratified flows. The distances between the three WMCSs were adjusted to capture radial and axial liquid dispersion by following tracer transport between sensors or between pairs of reading points from transmission and reception planes. Whichever tracer injection modality, the instantaneous pixel permittivity signals were corrected for baseline, then cross-sectionally averaged and normalized.

## Results and Discussion

### Flow regime

Flow regimes in the packed column submitted to the motion modalities described in Table 2, including the static vertical and inclined positions, were first delineated for a range of liquid superficial velocities,  $U_L$ , by analyzing the statistical behavior of the liquid saturation time series registered by the wire mesh sensors. The transition point demarcating replacement of one flow regime by another was

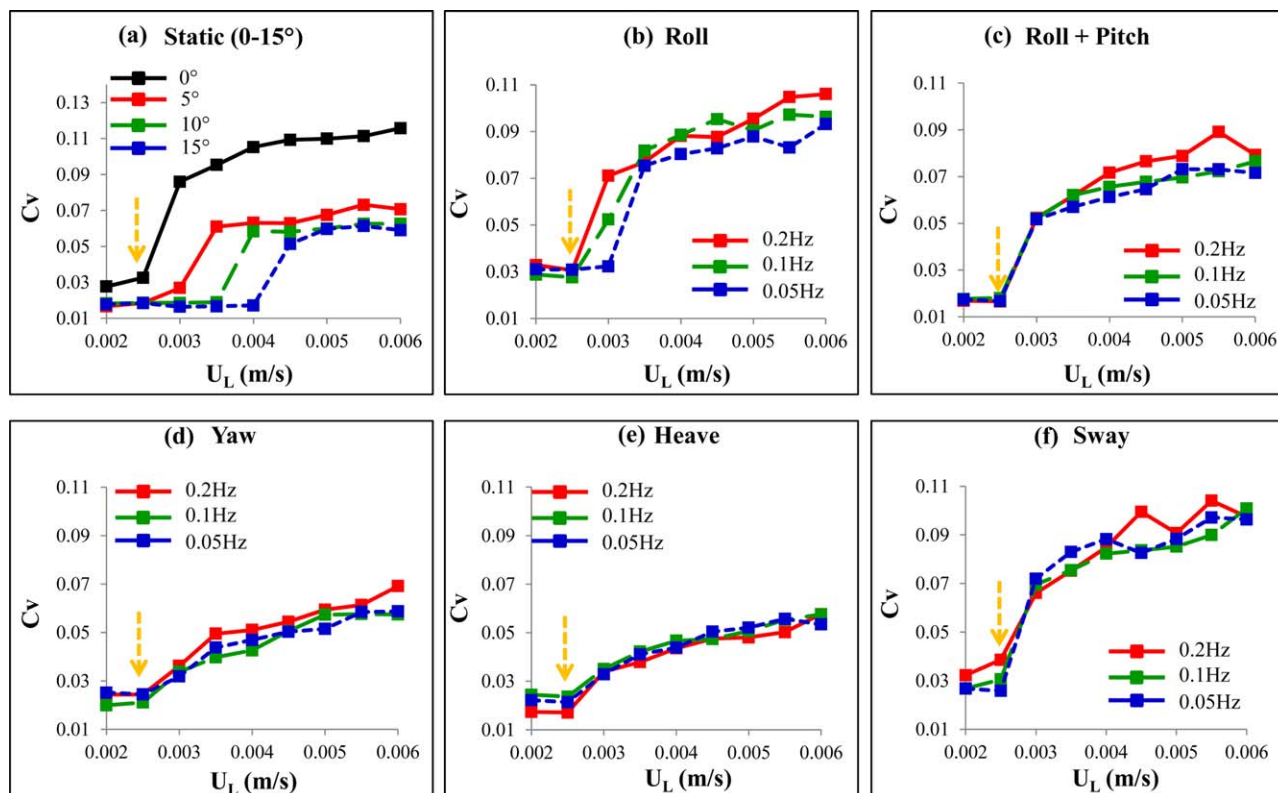


**Figure 4. Demarcation of trickle, and segregated/trickle and pulse flow regimes from plots of the coefficient of variation vs. liquid superficial velocity.**

Arrow marks position of transition (a) vertical/slanted beds, (b) roll, (c) roll + pitch, (d) yaw, (e) heave, and (f) sway. [Color figure can be viewed in the online issue, which is available at [wileyonlinelibrary.com](http://wileyonlinelibrary.com).]

identified from plots of the coefficient of variation ( $C_v$ ) of the cross-sectionally averaged liquid saturation time series as a function of  $U_L$ . The coefficient of variation was computed in the usual manner as the ratio of the signal standard deviation normalized by the time-average liquid saturation.<sup>40</sup>

For illustration, regime changeover highlighted with an arrow in Figure 4 was identified from  $C_v$  plots by sweeping the [2–6] mm/s  $U_L$  range at 0.5 mm/s increments at constant gas superficial velocity  $U_G = 32$  mm/s for the static vertical and slanted beds (a), and for the motion scenarios: roll (b), roll + pitch (c), yaw (d), heave (e), and sway (f). Supported by visual observations, trickle and segregated/trickle flow regimes entrenched in the left-most regions of the  $C_v$ - $U_L$  plots. There, while exhibiting the lowest values,  $C_v$  remained indifferent to  $U_L$  variations up to the transition point. A post-transition pulse flow regime took over as confirmed from visual observations in accordance with which  $C_v$  increased monotonically with liquid superficial velocity.

In the static positions, a shift of transition point to higher liquid velocities took place with increasing the column tilt angle (Figure 4a). For instance at  $U_G = 32$  mm/s, the vertical-column trickle flow ( $U_L < 2.5$  mm/s) region was stretched up to  $U_L < 3, 3.5,$  and  $4$  mm/s at  $5^\circ, 10^\circ,$  and  $15^\circ$  inclination angles, respectively. Broadening of the low-interaction domain toward higher liquid loads as the bed was tilted coincided with the emergence of a stratified (segregated/trickle)<sup>15</sup> flow regime where liquid-rich and gas-rich regions occupied, respectively, the lower and upper regions of the bed hence conceding on the intensity of gas-liquid interactions. Moreover, the declining trend of  $C_v$ , that is, relative strength of liquid saturation fluctuations, with tilt angle

in the pulse flow regime revealed the persistence of some degree of stratified flow to allay gas-liquid interactions.<sup>15</sup>

Examination of the flow regimes after the column was submitted to the various hexapod motion excitations (Table 2) revealed a notable restriction in the variability of the transition point, clustering around about 2.5–3 mm/s for all motions at  $U_G = 32$  mm/s (Figures 4c–f) while being quite close to that identified in the case of the static vertical column (Figure 4a). As far as the intensity of gas-liquid interactions is echoed through high  $C_v$  values, yaw whereby the vertical column oscillated around its revolution axis (Figure 4d, Supporting Information Appendix A) or likewise heave for which the vertical column moved up and down (Figure 4e, Supporting Information Appendix A) featured lesser active pulse flow regime than the static vertical configuration (Figure 4a) over the same fluid throughput ranges. Conversely, sway (Figure 4f, Supporting Information Appendix A) more or less replicated the  $C_v$ - $U_L$  behavior of the static vertical configuration (Figure 4a) as might apparently be conceived from the neutrality of horizontal column gentle periodic displacements. Finally, as suggested from Supporting Information Appendix A for the roll and roll + pitch motions (Figures 4b, c), it is conceivable that the inertial forces prompted by the robot acceleration contributed to reinforce the trickle-flow liquid film structures and to upset the gravity-driven stratification the manifestation of which was the strongest at the approach of the extreme inclination positions, that is,  $\pm 15^\circ$ . This interpretation is reinforced by the delayed pulse flow at the lowest roll frequency on account of the broadest segregated/trickle region identified for the static  $15^\circ$  inclined bed (Figure 4a).

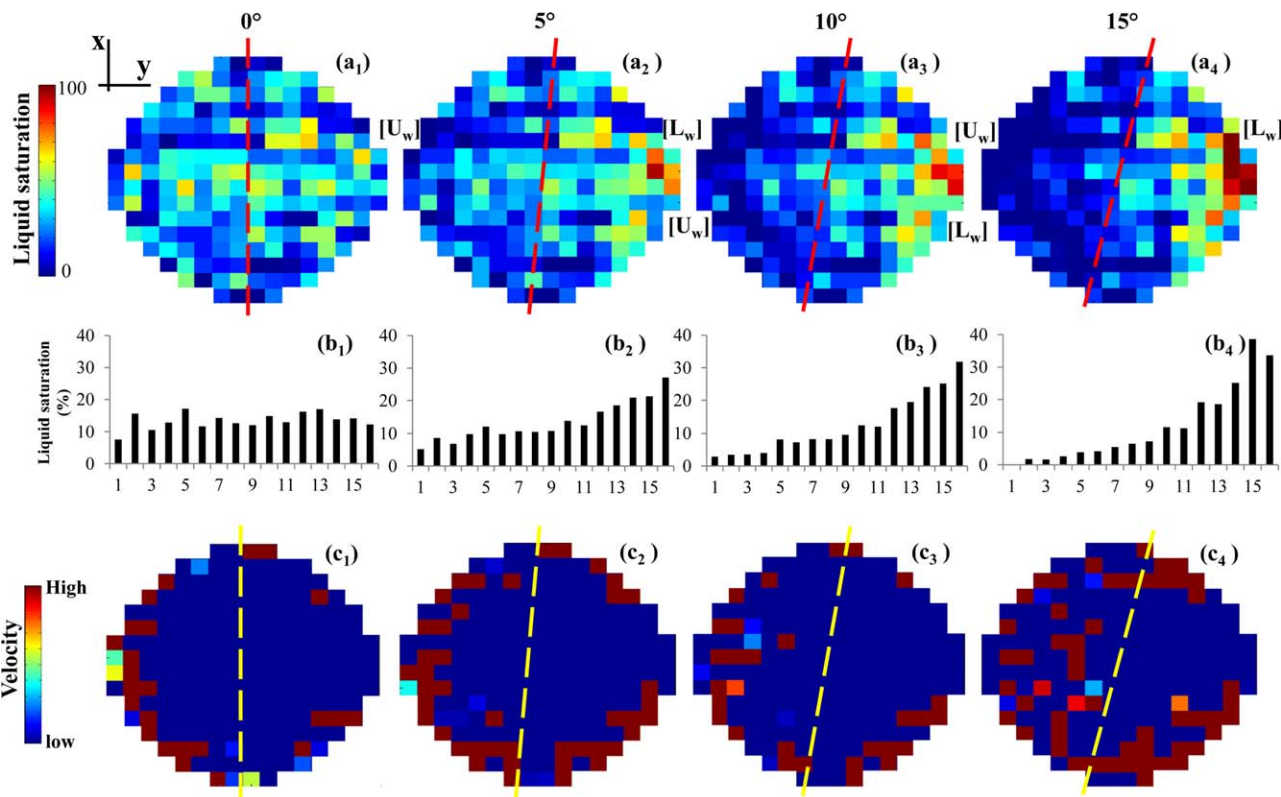


**Figure 5.** (a) 2-D time-average free-drained liquid saturation distribution at bed height ca. 63 cm as a function of column tilt angle (shown as red dotted line), [U<sub>w</sub>] = uppermost, [L<sub>w</sub>] = lowermost column, (b) transverse profile of y-direction-averaged liquid saturation, and (c) two-plane cross-correlation analysis of liquid saturation time series highlighting the fast and slow velocity events to delineate stratified flow boundaries.

[Color figure can be viewed in the online issue, which is available at [wileyonlinelibrary.com](http://wileyonlinelibrary.com).]

Subsequently, the set of superficial velocities  $U_L = 2$  mm/s and  $U_G = 32$  mm/s, corresponding to trickle or segregated/trickle flow regimes for the tested hexapod modalities, was retained for the subsequent gas-liquid distribution and tracer studies.

### Gas-liquid distribution

**Static Column.** 2-D pixel-affixed temporal averages of dynamic liquid saturation are shown in Figures 5a<sub>1-4</sub> as a function of column tilt angle for the static bed. Lower (right) and upper (left) levels in these 2-D contours were, respectively, identified with [L<sub>w</sub>] and [U<sub>w</sub>] in Figures 5a<sub>2-4</sub>. The readings from three wire mesh sensors located at bed heights 60, 61.2, and 66.2 cm were found to differ marginally and by no more than 0.37% on pixel basis. To highlight the breakdown of symmetry in liquid distribution due to bed inclination, the liquid saturation data of Figures 5a<sub>1-4</sub> were line-averaged along  $x$ -axis and plotted as a function of  $y$  in Figures 5b<sub>1-4</sub>. As seen from both figure sets, a quasi-even liquid distribution was achieved for the static vertical bed. However, inclining the bed by 5°, 10°, and 15° at given gas and liquid throughputs led to the appearance and development of permanent segregation zones in agreement with previous studies' observations on the change of trickle flow regime into a segregated/trickle flow as soon as a critical tilt angle of about 5°–6° was reached.<sup>15</sup> Note that the upper gas-rich region was not always devoid of liquid; likewise, the lower liquid-rich region was not gas-free even though their

tendency was to evolve toward single-phase regions as tilt angle increased (Figures 5a<sub>2-4</sub>).

2-D maps of local velocity events were also computed from a cross-correlation analysis of the instantaneous pixel-paired liquid saturations obtained by means of the twin wire mesh sensor (WMSC<sub>1</sub>/WMSC<sub>2</sub> separation distance of 12 mm). Velocity plots displayed in Figures 5c<sub>1-4</sub> as fast and slow events corresponded to Figures 5a<sub>1-4</sub> experiments. Soundly inherent with the notion of rapid incursions of liquid in the bed highest-permeability region dominated by gas occupancy ( $U_G/U_L = 16$ ), the fastest phase saturation fluctuations as detected by means of the twin sensor befell mostly nearby the walls for the vertical bed (Figure 5c<sub>1</sub>). It can also be seen from the 2-D velocity maps of Figures 5c<sub>1-4</sub> that by increasing the bed tilt angle to 15° magnified progressively the velocity-active region which appeared to except the lower liquid-rich region identified in Figure 5a<sub>4</sub> with stratified gas-liquid flow. This latter, because of lack of propagating perturbations in the twin sensor field of view, was coherent with a gas-free liquid lower stratum. On the contrary, liquid islands in the gas-rich region caused observable phase fluctuations and thus allowed detecting velocity events by the sensor.

To ease subsequent discussions on the dynamics of gas-liquid segregation under the aforementioned hexapod motion modalities, it was judged pertinent to define a criterion for the assessment of the degree of uniformity over the bed cross-section to highlight departures of the liquid saturation distribution from an ideal distribution as the one that should

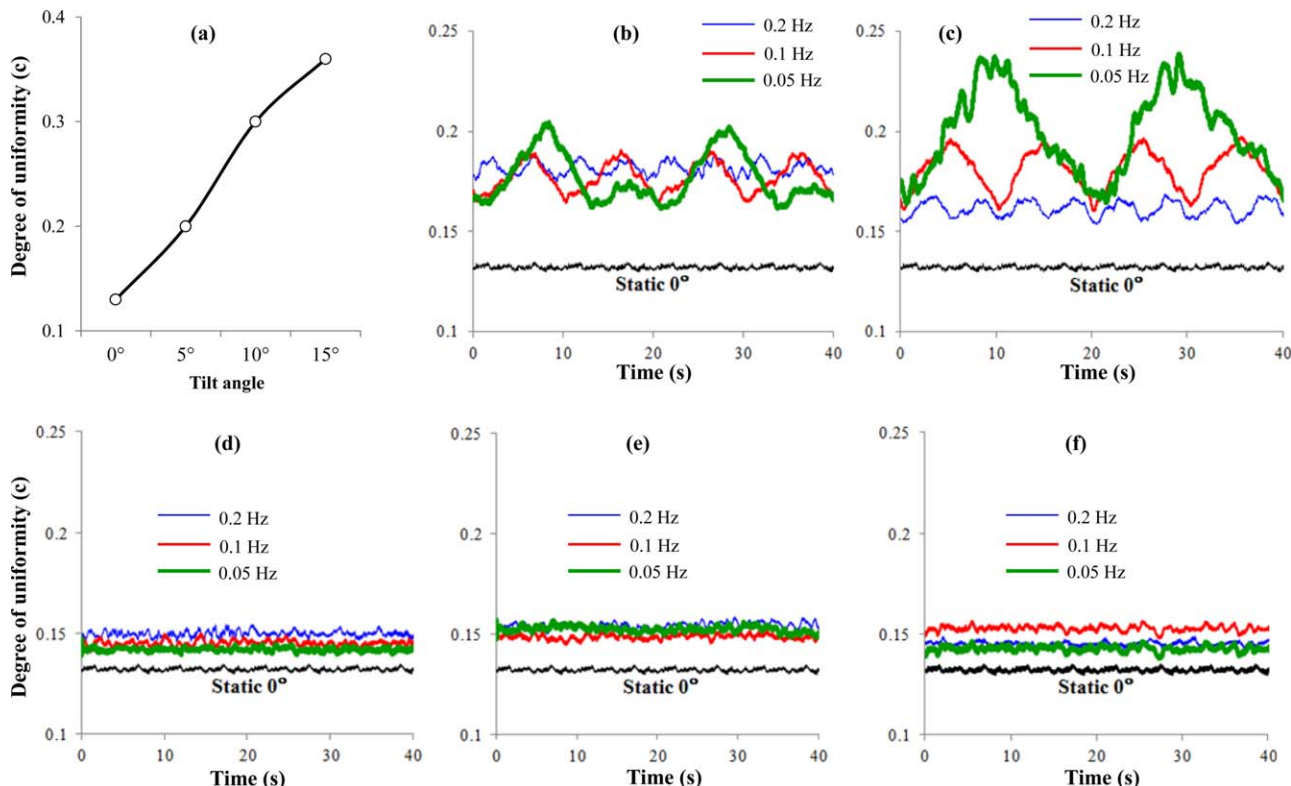


**Figure 6.** Effect of packed bed tilt angle and motion on the degree of uniformity criterion,  $\chi$ : (a) static inclination, (b) roll, (c) roll + pitch, (d) yaw, (e) heave, and (f) sway.

[Color figure can be viewed in the online issue, which is available at [wileyonlinelibrary.com](http://wileyonlinelibrary.com).]

prevail in static vertical beds subject to even initial liquid distribution ( $\chi = 0$ ). A degree of uniformity was defined as  $\chi = n^{-1} \sum (\beta_i - \langle \beta \rangle)^2 / \langle \beta \rangle^2$ , where  $n$  is the number of pixels per cross-section,  $\beta_i$  is the time-average liquid saturation corresponding to  $i$ -th pixel and  $\langle \beta \rangle = n^{-1} \sum \beta_i$  is the liquid saturation averaged over all the cross-section pixels.

According to this criterion, Figure 6a confirms the degradation of liquid distribution with column tilt; the lowest  $\chi$  value being achieved in vertical position while it nearly quadrupled at a tilt of  $15^\circ$ . The fact that  $\chi$  was not much closer to the theoretical zero value in the vertical station was attributed to the sensitivity of  $\chi$ , on one hand, to sensor invasiveness which might perturb the local bed porosity due to geometric mismatch of the beads-wire mesh neighborhood, and conversely, to small imperfections in the liquid feed on the bed top that might have led to the line-average liquid saturation profile highlighted in Figure 5b.<sup>41,42</sup>

**Moving Column.** During the hexapod movements and as presented in Figures 6b–f,  $\chi$  instantaneous values were clearly impacted by the motion frequency and even resulted, for the rotating types of motion, in nonmonotonic behaviors. Indeed, both roll and roll + pitch motions induced noticeable periodic variations of  $\chi$  which evolved consistently with the hexapod rotational frequencies. This was unlike the yaw, heave, and sway motions which, regardless of the imposed frequency, barely affected the degree of uniformity,  $\chi$  (Figures 6d–f) although revealing a slight bias as compared with the vertical static configuration (Figure 6a). In general, prompting vessel motion degraded the quality of the gas-liquid distribution with staggering effects attributed to the rotational degrees of freedom contrary to the translational episodes.

Over one-half roll period, the column continuous tilting from  $+15^\circ$  to  $0^\circ$  and then to  $-15^\circ$  correspondingly reflected in the degree of uniformity highest degradation (maximum, Figure 6b) evolving toward the vertical position lowest  $\chi$  (minimum, Figure 6b) before deteriorating once again after the column completed half a cycle. Resumption of such sequence reproduced the oscillating behavior of the degree of uniformity shown in Figure 6b. Representative video animations of the gas-liquid flow maldistribution in the packed column subject to roll motion at different frequencies are displayed in the Supporting Information (Appendix B). Higher frequency roll motion tended to smooth out the discrepancies in phase distribution, probably as a result of stronger inertial forces, although the average trend of the degree of uniformity tended to drift far off that of the static vertical configuration. It is worthy of notice that the maxima and minima reached by  $\chi$  were roll frequency-dependent. Hence, the lower the roll frequency, the more these  $\chi$ -extrema tended to approach both the measured static inclined (lower uniformity) and static vertical (higher uniformity)  $\chi$  values of Figure 6a. At any rate, this trend was in agreement with the intuitive notion that gentler roll motions were to induce temporarily more defined flow patterns inside the bed. By extension to floating systems, slower roll motions would probably inflict more severe deterioration of gas-liquid distribution than faster ones as highlighted by the largest contrasts of the degree of uniformity as roll frequency decreased (Figure 6b). However, the oscillation magnitude in the degree of uniformity is likely to be column-diameter-dependent. The wall, matter-of-factly, plays a crucial baffling role in the restriction of the gravity-driven migration of liquid and is thus necessary in prompting gas-liquid segregation

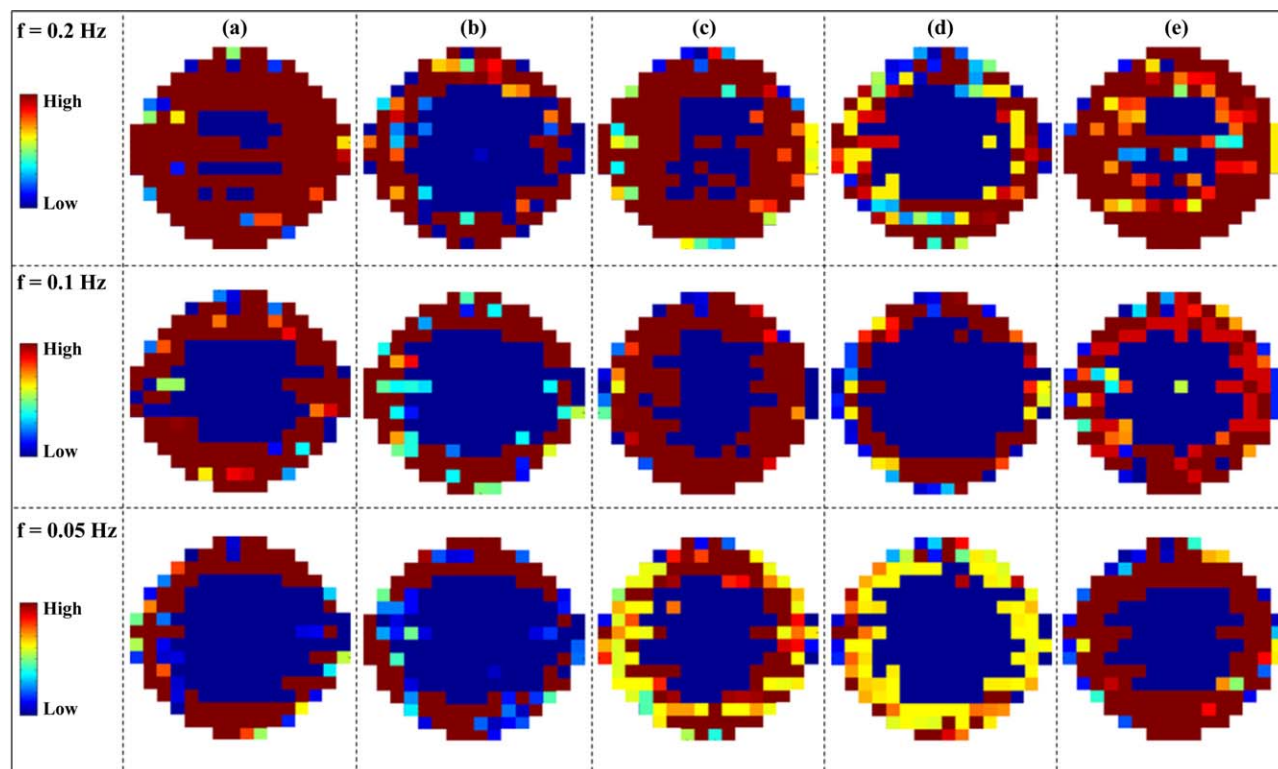


**Figure 7. Two-plane cross-correlation analyses of liquid saturation time series highlighting the fast and slow velocity events under (a) roll, (b) roll + pitch, (c) yaw, (d) heave, and (e) sway motions.**

[Color figure can be viewed in the online issue, which is available at [wileyonlinelibrary.com](http://wileyonlinelibrary.com).]

as discussed earlier. Larger columns, therefore, are expected to showcase, at least under low liquid loadings as in trickle flow regime, less spectacular contrasts in terms of gas-liquid maldistribution. This anticipation builds on the fact that for given roll frequency and gas/liquid flow rate ratio, small columns due to their wall confinement face more severe segregation than larger ones owing to the reduced transit time for the liquid to reach the vessel walls. However, the relationship between vessel diameter and gas-liquid maldistribution justifies in itself a dedicated study which was beyond this study's scope.

The roll + pitch motion likewise showed greater irregularities in phase distribution at the lower frequencies leading to the highest contrasts in  $\chi$  values (Figure 6c). This was attributed to the fact that liquid and gas gradually interchanged their positions along the lower wall for a column often off-vertical position due to the  $90^\circ$  phase lag between roll and pitch thus inciting fewer phase mixing events. However, unlike roll motion, high frequencies of roll + pitch motion tended to improve gas-liquid distribution (low  $\chi$ ) owing to greater gas-liquid mixedness prompted by the alternating takeover of roll and pitch. Video animations of the gas-liquid flow maldistribution in the packed column subject to roll + pitch motion illustrate these interpretations (see Supporting Information, Appendix C).

2-D maps of local velocity events, akin to those discussed previously for the static inclined beds (Figure 4), were also obtained from a cross-correlation analysis of the instantaneous pixel-paired liquid saturations for the roll, roll + pitch, yaw, heave, and sway motions. Using the same rationale as above, the velocity plots, correspondingly displayed in Figures 7a–e as a function of frequency, allowed sensing the

extent and intensity of traffic between gas and liquid at given pixels as fast and slow events. Roll (Figure 7a), yaw (Figure 7c), and sway (Figure 7e) motions often highlighted the highest activities across the widest regions in the 2-D contour plots, especially at higher frequencies. The faster robot turnover brought about more frequent zigzag and crisscrossing in fluid trajectories; in short, yielding more gas-liquid mixing and promoting more frequent encounters of liquid with the faster gas flow. However, a lower activity associated with roll + pitch (Figure 7b) and heave (Figure 7d) motions was noticeable even though it was still higher than that observed under static configurations and generally gaining strength as motion frequencies increased from 0.05 to 0.2 Hz.

### Liquid dispersion

*Static Column.* To recognize the dispersive phenomena occurring as a result of tilting the packed bed, tracer pulses were injected according to the integral protocol described earlier: two sensors located in the bed first quarter and third one placed in the last quarter, see Figure 3a. The tracer signals registered by WMCS<sub>1</sub>, WMCS<sub>2</sub>, and WMCS<sub>3</sub> in the static vertical ( $a_1$ ) and slanted ( $a_{2-4}$ ) positions from  $5^\circ$  to  $15^\circ$  are illustrated in Figure 8a. Perceptible on the signals were shoulder and skewness features reminiscent of a two-zone residence time distribution pattern (Figure 8a<sub>2</sub>: WMCS<sub>3</sub> for  $5^\circ$ , Figure 8a<sub>3</sub>: WMCS<sub>1-3</sub> for  $10^\circ$  tilt angles) in accordance with the phase segregation objectified earlier (Figures 5a and 6a). The tracer tests revealed that tracer migration in the lowermost liquid-rich region outpaced the one slowly drifting in the uppermost gas-rich region, respectively, labeled as [L<sub>w</sub>] and [U<sub>w</sub>] in Figures 8a<sub>2, 3</sub>. It was the persistence of

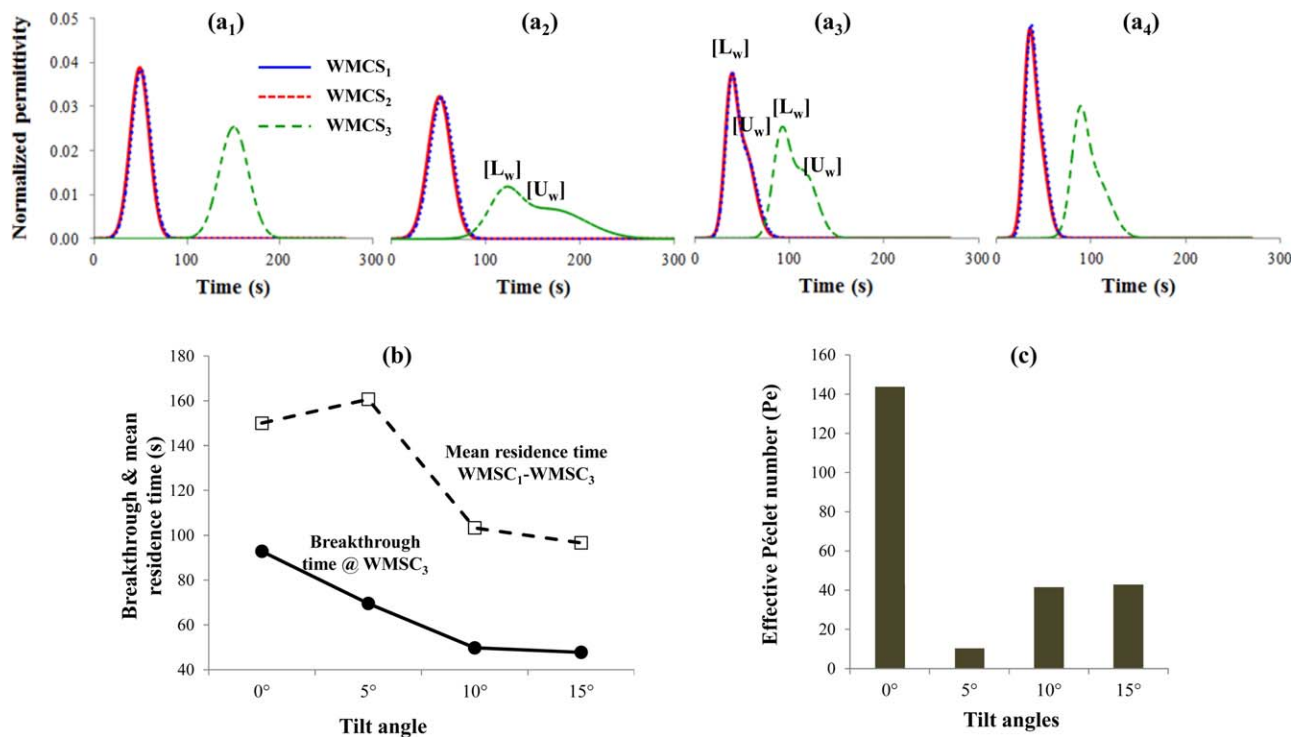


**Figure 8.** Tracer responses sensed by WMCS<sub>1</sub>, WMCS<sub>2</sub>, and WMCS<sub>3</sub> in static vertical (a<sub>1</sub>) and 5° (a<sub>2</sub>), 10° (a<sub>3</sub>), and 15° (a<sub>4</sub>) slanted packed bed following an upstream pulse injection at  $t=0$  as shown in Figure 3a, [U<sub>w</sub>] = uppermost, [L<sub>w</sub>] = lowermost column (b) bed inclination vs. breakthrough time for the fastest liquid tracer stream to travel from WMCS<sub>1</sub> to WMCS<sub>3</sub> levels and for liquid mean residence time up to WMCS<sub>3</sub> height, (c) bed inclination vs. liquid effective axial Péclet number.

[Color figure can be viewed in the online issue, which is available at [wileyonlinelibrary.com](http://wileyonlinelibrary.com).]

liquid islands percolating through the pores in the gas-rich region that caused the distinctive shoulder and skewness for 5° and 10° bed inclinations. However, the shoulder almost vanished at 15° (Figure 8a<sub>4</sub>) after the majority of permissible liquid flow paths were redirected along the column lower wall because phase segregation was virtually complete as can be assessed from the liquid saturation contour plots shown in Figure 5a<sub>4</sub>.

The effect of bed inclination on the breakthrough time for the fastest liquid tracer stream to travel from WMCS<sub>1</sub> to WMCS<sub>3</sub> levels and of the liquid mean residence times to reach WMCS<sub>3</sub> measurement location is illustrated in Figure 8b. In general and as expected, phase segregation resulted in lower breakthrough times and lower mean residence times. Furthermore, the inflated signal variances revealed in Figures 8a<sub>2-4</sub> suggest drastic departures from liquid plug flow due to bed inclination. To get a sense of these deviations, an axial dispersion model with open–open boundary conditions was used to describe the liquid residence time distribution and an effective Péclet number was fitted using the well-established Aris's method and time-domain nonlinear fitting.<sup>43,44</sup> Figure 8c portrays the dramatic collapse in the values of Péclet numbers with column tilting relative to the static vertical bed. The onset of phase segregation under 5° tilt angle led to the most severe liquid dispersion as evidenced from WMCS<sub>3</sub> signal variance in Figure 8a<sub>2</sub>. Further increase in tilt angle led to a slight increase of Péclet number although far from nearing the one achieved for the static vertical bed. A key outcome from this tracer tests is that inclined beds, *ceteris paribus*, would achieve a lower performance in terms of reaction or mass-transfer efficiency as compared with

static vertical beds owing to a dramatic loss in gas-liquid contacting because of stratification and further departure from liquid plug flow pattern.

To further highlight the liquid displacement structure after phase segregation had taken place, tracer pulses were also injected according to the local protocol. Figure 9 shows the tracer responses as a function of bed inclination angle for the three wire mesh sensor positions with injection points near WMCS<sub>1</sub> as sketched in Figure 3b. It is noteworthy that for the vertical bed, the shoulder/asymmetry appearing in WMCS<sub>3</sub> signals with diametrically opposed injections (left and right as shown, respectively, in Figures 9a<sub>1</sub>, c<sub>1</sub>), unlike the more symmetric response from central injection (Figure 9b<sub>1</sub>), was symptomatic of a preferential flow in the bed highest-permeability region. As highlighted earlier, this aspect conforms to the fastest phase saturation fluctuations near the walls for the vertical bed (Figure 5c<sub>1</sub>). Notwithstanding and unambiguously visible from WMCS<sub>3</sub> signals for inclined bed, the injection of tracer near the upper wall (Figures 9a<sub>2-4</sub>) restored the skewness and shoulder previously diagnosed with the integral injections. Long-lasting skewness was particularly manifest with increasing column tilt angle. The centerline tracer injections exposed shoulder-free bell-shaped responses which widened with tilt angle (Figures 9b<sub>2-4</sub>). The nonappearance of a clear shoulder with centerline injections was attributed to the gravity-driven radial flow and nearness of tracer injection with the liquid-rich lowermost region facilitating the passage of the major part of the tracer toward the lower wall. Finally, tracer injections in the lower wall region resulted in signals with markedly thinner variances particularly with increasing column

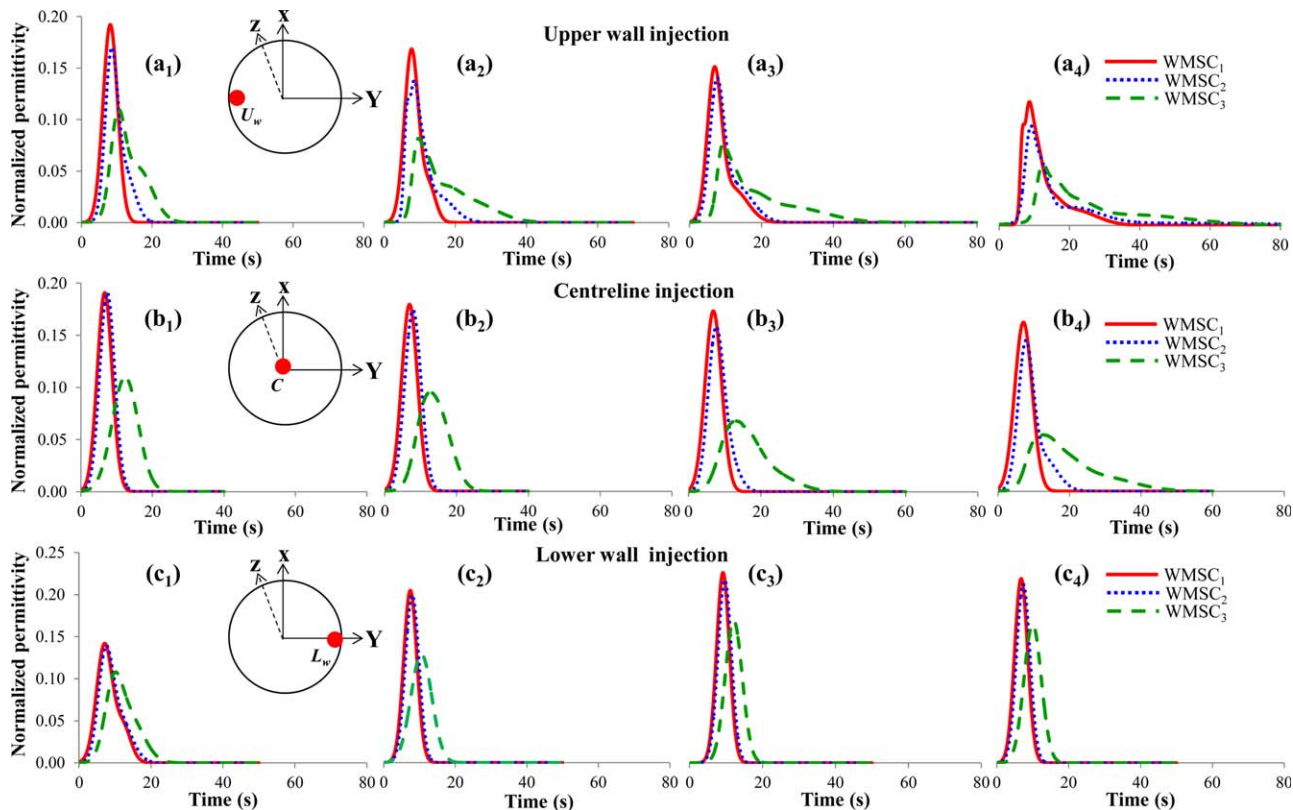


**Figure 9.** Local tracer responses sensed by WMCS<sub>1</sub>, WMCS<sub>2</sub>, and WMCS<sub>3</sub> as a function of bed inclination and origin of tracer injections (a) upper wall, (b) centerline, and (c) lower wall:  $\alpha_1 = 0^\circ$ ,  $\alpha_2 = 5^\circ$ ,  $\alpha_3 = 10^\circ$ ,  $\alpha_4 = 15^\circ$  where  $\alpha = a, b, \text{ or } c$ .

[Color figure can be viewed in the online issue, which is available at [wileyonlinelibrary.com](http://wileyonlinelibrary.com).]

tilt angle (Figures 9c<sub>2-4</sub>). This reflected, as discussed earlier, in shorter breakthrough and mean residence times that were symptomatic of the poor transverse mixing of the tracer with the liquid islands belonging to the gas-rich upper-wall region.

**Moving Column.** The tracer spread behavior as influenced by the column movements defined in Table 2 was examined next. Examples of tracer responses for the column subject to different roll frequencies are illustrated in Figure 10a for the WMCS<sub>2</sub> and WMCS<sub>3</sub> measurement regions following the integral protocol. Tracer responses for the static vertical and 15° inclined bed arrangements were also shown for comparison. Tracer displacements under column oscillations and in static inclined configuration definitely differed from one another (Figure 10a). Interestingly, regardless of roll frequency, the signal modes and shapes remained more or less consistent with those corresponding to the static vertical bed. However, liquid flow became more dispersive on setting column roll motions as exposed from the inflating signal variances (Figure 10a). Such a qualitative loss of plug-flow character was also observed whichever hexapod's degree of freedom was actuated. This is depicted in Figure 10b in which the impact of frequency on the effective Péclet number was captured for the roll, roll + pitch, heave, sway, and yaw motions. For comparison, the value of Péclet number for the static vertical bed is also shown. Specifically, a decreasing frequency translated to a reduction of Péclet number. Yaw was an exception probably because the faster the tangential movements the more efficient the transverse homogenization of tracer concentration. Furthermore, as frequency diminished, the tendency of dispersion for the

rotational motions, that is, roll and roll + pitch, was to approach the dispersion worst case scenario achieved in static inclined beds (Figures 8c and 10a). Finally, among the tested motions, heave featured the lowest Péclet numbers which intuitively can be linked with the extra axial dispersion triggered by the vertical piston-like course of the column.

Tracer centerline injections following the local protocol (Figure 3b) divulged further insights on the mixing details imprinted on the liquid flow for each type of tested column motion. A degree of transverse homogeneity of the tracer concentration field was defined as the permittivity variance computed, for each instant, over the ensemble of pixels belonging to sensed downstream plane, here WMCS<sub>3</sub> plane. Perfect transverse homogeneity, that is, tracer homogenous concentration field, is tantamount to zero variance while poor transverse dispersion reflects in more or less important variance values depending on the significance of permittivity (or tracer concentration) contrasts among pixels. Figure 11 summarizes the various instantaneous variance patterns following a brief tracer pulse for the roll (a), roll + pitch (b), yaw (c), heave (d), and sway (e) motions. The variance response corresponding to the static vertical column was also drawn for comparison. In addition, representative video animations of the tracer wanderings corresponding to each type of motion were gathered in the Supporting Information (Appendix D).

On account of the nature of the single initial tracer pulse, the variance profiles characterizing the roll (Figure 11a) and roll + pitch (Figure 11b) motions were very unusual reflecting in a series of frequency-dependent dampening peaks.

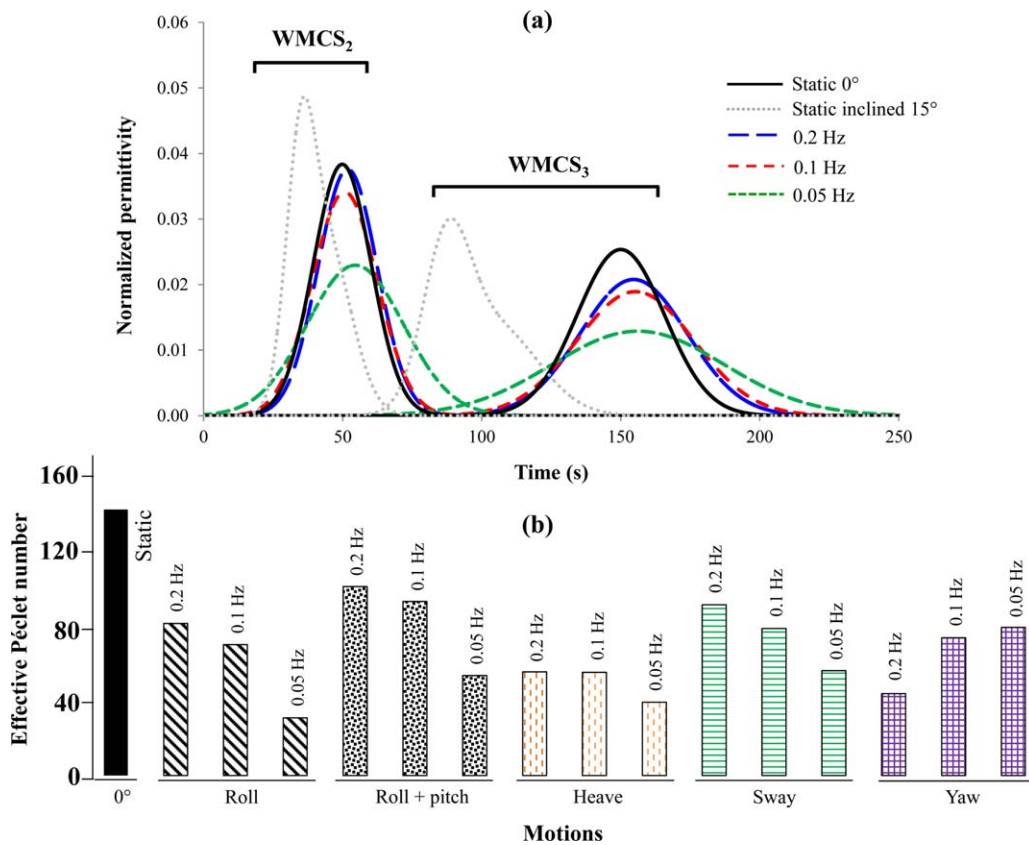


Figure 10. Tracer responses sensed by WMCS<sub>2</sub> and WMCS<sub>3</sub> (pulse injection according to integral protocol, Figure 3a) under roll motion as a function of frequency (a) hexapod motion frequency vs. liquid effective axial Péclet number (b).

[Color figure can be viewed in the online issue, which is available at [wileyonlinelibrary.com](http://wileyonlinelibrary.com).]

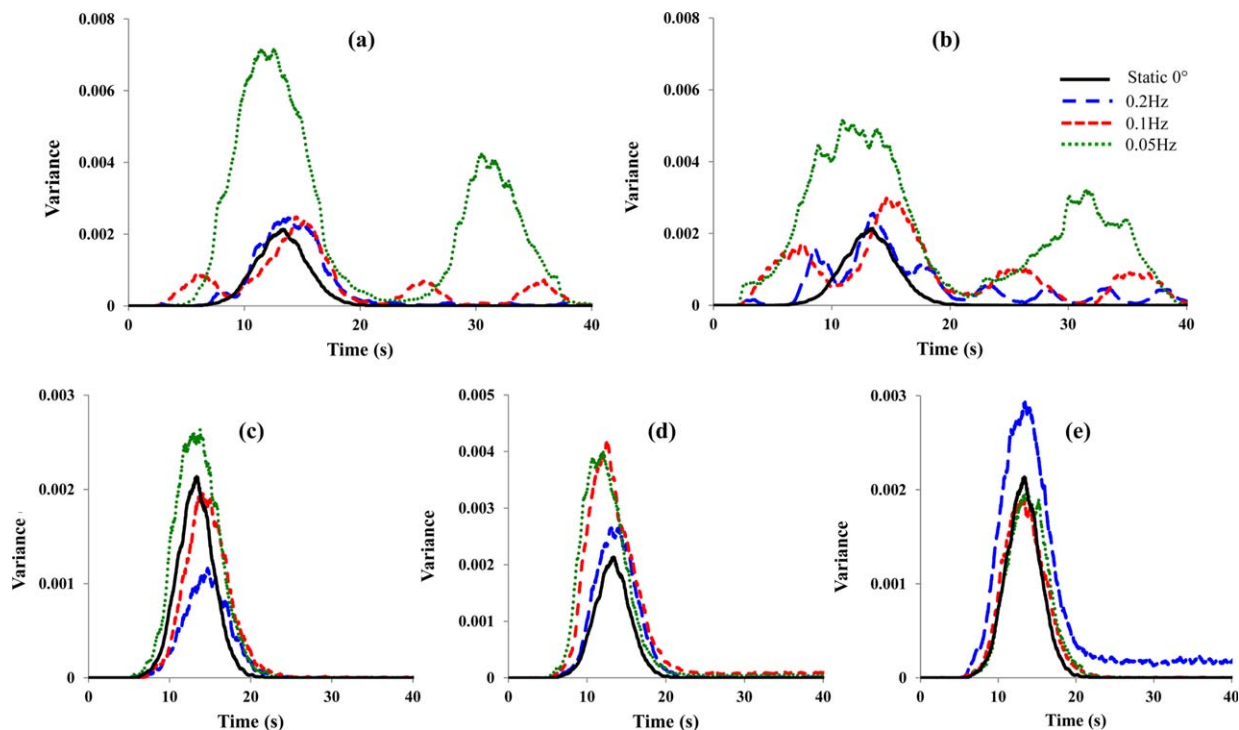


Figure 11. Degree of transverse homogeneity assessed from permittivity variance on WMCS<sub>3</sub> plane (pulse injection according to local protocol, Figure 3b) for roll, roll + pitch, yaw, heave, and sway packed column motions for different frequencies.

[Color figure can be viewed in the online issue, which is available at [wileyonlinelibrary.com](http://wileyonlinelibrary.com).]

Examination of the video animations for the roll and roll + pitch excitations (Supporting Information Appendix D) indicates that peak splitting was the result of transverse zig-zag (roll) or swirl (roll + pitch) motions of the tracer. The maximum variance in Figure 11a characterized tracer migration toward the lowermost ( $L_w$ ) region of the column in response to tilting whereas the minimum variance occurred during centerline crisscrossing of the tracer cloud at the approach of column verticality. During roll + pitch motion, liquid migration toward the lower wall led to one tracer spot, that is, high variance (Figure 11b). Conversely, the slower liquid flow conveyed by the gas spread by percolation in the column center leading to much more dispersed tracer spots, that is, low variance. Tracer animations revealed that the lower the roll (or roll + pitch) frequency, the poorer the transverse dispersion reflecting in the inflated variances in Figures 11a, b. Likewise, tracer elution to be completed was much longer which was interpreted as resulting from increased axial dispersion with decreasing roll (or roll + pitch) frequency. Unlike the two previous cases, no tracer segregation occurred in the case of yaw and heave motions (Figures 11c, d) and the corresponding tracer elution history was qualitatively similar to that of the static vertical bed (Supporting Information Appendix D). As indicated by the variance shoot up, the decrease in yaw or heave frequency came along with a lower radial dispersion. Heave motion however, promoted more axial dispersion as discussed earlier (Figure 10b). In terms of frequency trend, the sway motion featured exactly the opposite of yaw and heave (Figure 11e), that is, lower radial but higher axial dispersion with increasing frequency.

## Conclusion

Gas-liquid cocurrent downflow in slanted and moving packed beds was studied with the aim to gain insights on the impact of sea swells on the performance of offshore treatment units. To mimic scrubbers/reactors embarked on floating production systems, a laboratory-scale packed bed was mounted on an hexapod ship motion simulator which was subject to sinusoidal excitations of single and combined degrees of freedom, namely, translations (surge or sway, heave) and rotations (roll or pitch, yaw, roll + pitch) in the 0.05–0.2 Hz frequency range. Three WMCS inserted at various heights along the packed bed were used to measure the local instantaneous liquid saturation and velocity. Hydrodynamic indicators were defined to assess the flow regimes, the fluid maldistribution, and the tracer radial and axial dispersion along the bed. The time-varying hydrodynamic behavior of the moving packed bed was also compared with that corresponding to the static vertical and inclined configurations.

The following conclusions were drawn:

All motions induced a worsening of phase maldistribution compared with the static vertical bed. Tilting motions (roll, roll + pitch) led to significant frequency-dependent gas-liquid segregation. Low-frequency motions prompted a sequence of large and low maldistribution oscillations owing to the aggravated phase segregation at the short-lived slanted positions and to the improved phase distribution at the evanescent vertical position while high-frequency motions smoothed out maldistribution discrepancies. Nontilting motions (heave, yaw or surge, sway) led to frequency-indifferent maldistribution yet slightly exceeding the ones prevailing under stationary vertical configuration.

The liquid flow became more dispersive during motion leading to a reduction of the effective axial Péclet number as frequencies decreased. Secondary liquid circulations were induced by the moving column, that is, crosswise zigzag for roll, and swirl for roll + pitch. Yaw and heave motions exhibited qualitatively similar liquid dispersion to that of stationary vertical columns.

A lower performance in terms of reaction or mass-transfer efficiency would be expected in inclined and moving packed beds as compared with stationary vertical beds on account of aggravated phase segregation and inflated liquid dispersion.

## Acknowledgments

The authors gratefully acknowledge the Natural Sciences and Engineering Research Council of Canada and the Canada Research Chair on Sustainable Energy Processes and Materials for their financial support.

## Literature Cited

1. El-Reedy MA. Introduction to offshore structures. In: El-Reedy MA, editor. *Offshore Structures: Design, Construction and Maintenance*. Oxford, UK: Gulf Professional Publishing, Elsevier Inc., 2012:1–21.
2. Shimamura Y. FPSO/FSO: state of the art. *J Mar Sci Tech Jpn*. 2002;7(2):59–70.
3. Leffler WL, Pattarozzi R, Sterling G. A century getting ready. In: Leffler WL, Pattarozzi R, Sterling G, editors. *Deepwater Petroleum Exploration & Production: A Nontechnical Guide*, 2nd ed. Tulsa, OK: PennWell Books, 2011:1–30.
4. International energy agency. *World Energy Outlook 2010*, Available at: [www.worldenergyoutlook.org/publications/weo-2010/](http://www.worldenergyoutlook.org/publications/weo-2010/).
5. Halkyard J. Floating offshore platform design. In: Chakrabarti SK, editor. *Handbook of Offshore Engineering*, Vol. 1. Oxford, UK: Elsevier Inc, 2005:419–662.
6. Offshore magazine, deepwater solutions & records for concept selection: going deeper with production technology. 2012;72. Available at: [http://www.offshore-mag.com/content/dam/offshore/print-articles/Volume%2072/may/0512OS\\_DeepwaterPoster040512Ads.pdf](http://www.offshore-mag.com/content/dam/offshore/print-articles/Volume%2072/may/0512OS_DeepwaterPoster040512Ads.pdf).
7. Reinicke KM, Hueni G, Liermann N, Oppelt J, Reichetseder P, Unverhaun W. Oil and gas, 7. Production. *Ullmann's Encyclopedia of Industrial Chemistry*. John Wiley & Son's, Inc., 2014:1–64.
8. Duduković MP, Larachi F, Mills PL. Multiphase catalytic reactors: a perspective on current knowledge and future trends. *Catal Rev*. 2002;44(1):123–246.
9. Armstrong PA, Kalbassi MA, Miller D. Distributor for packed liquid-vapor contact column. CA Patent 2258406 C, 2002.
10. Kalbassi M, Zone I. Liquid distributor. US Patent 0020238 A1, 2004.
11. Haroun Y, Raynal L, Alix P. Dispenser tray for an offshore gas/liquid contact column with perforated walls. *EP Patent* 2653204 A1, 2013.
12. Duss M, Roza M. Columns subject to motion: Maldistribution sensitivity and susceptibility. In: *10th International conference on Distillation & Absorption*. Friedrichshafen, Germany, 2014:14–17.
13. Fraysse P, Werlen E. Floating marine structure. US Patent 6397630 B1, 2002.
14. Atta A, Schubert M, Nigam K, Roy S, Larachi F. Co-current descending two-phase flows in inclined packed beds: experiments versus simulations. *Can J Chem Eng*. 2010;88(5):742–750.
15. Schubert M, Hamidipour M, Duchesne C, Larachi F. Hydrodynamics of cocurrent two-phase flows in slanted porous media—modulation of pulse flow via bed obliquity. *AIChE J*. 2010;56(12):3189–3205.
16. Bouteldja H, Hamidipour M, Larachi F. Hydrodynamics of an inclined gas-liquid cocurrent upflow packed bed. *Chem Eng Sci*. 2013;102(11):397–404.
17. O'Dea D, Rudolph V, Chong Y, Leung L. The effect of inclination on fluidized beds. *Powder Technol*. 1990;63(2):169–178.
18. Valverde J, Castellanos A, Quintanilla M, Gilabert F. Effect of inclination on gas-fluidized beds of fine cohesive powders. *Powder Technol*. 2008;182(3):398–405.
19. Hudson C, Briens C, Prakash A. Effect of inclination on liquid-solid fluidized beds. *Powder Technol*. 1996;89(2):101–113.

20. Yakubov B, Tanny J, Maron DM, Brauner N. The dynamics and structure of a liquid–solid fluidized bed in inclined pipes. *Chem Eng J.* 2007;128(2):105–114.
21. Saez AE, Carbonell RG. Hydrodynamic parameters for gas–liquid cocurrent flow in packed-beds. *AIChE J.* 1985;31(1):52–62.
22. Holub RA, Dudukovic MP, Ramachandran PA. A phenomenological model for pressure-drop, liquid holdup, and flow regime transition in gas–liquid trickle flow. *Chem Eng Sci.* 1992;47(9–11):2343–2348.
23. Holub RA, Dudukovic MP, Ramachandran PA. Pressure-drop, liquid holdup, and flow regime transition in trickle flow. *AIChE J.* 1993;39(2):302–321.
24. Iliuta I, Larachi F, Al-Dahhan MH. Double-slit model for partially wetted trickle flow hydrodynamics. *AIChE J.* 2000;46(3):597–609.
25. Attou A, Ferschneider G. A two-fluid model for flow regime transition in gas–liquid trickle-bed reactors. *Chem Eng Sci.* 1999;54(21):5031–5037.
26. Zhao T, Liu K, Murata H, Harumi K, Takei M. Experimental and numerical investigation of particle distribution behaviors in a rolling circulating fluidized bed. *Powder Technol.* 2014;258:38–48.
27. Yasui T, Nakayama T, Yoshida K. Heat-transfer characteristics in a rocking fluidized bed. *Int J Heat Mass Transf.* 1984;11(5):477–488.
28. Nakanishi T, Nakai S, Kadota T, Furukawa T, Inoue S, Wakiyama Y, Yamada A. Experiments on performance of fluidized bed for marine use. *J Mar Eng Soc Jpn.* 1979;14:808–819.
29. Namie S, Osanai T, Yamanouchi H, Yokomura T. Investigation on fluidized bed combustion for marine application. *J Mar Eng Soc Jpn.* 1984;19:943–950.
30. Murata H, Oka H, Adachi M, Harumi K. Effects of the ship motion on gas–solid flow and heat transfer in a circulating fluidized bed. *Powder Technol.* 2012;231:7–17.
31. Zhao T, Liu K, Murata H, Harumi K, Takei M. Investigation of bed-to-wall heat transfer characteristics in a rolling circulating fluidized bed. *Powder Technol.* 2015;269:46–54.
32. Zeńczak W. Investigation of fluidized bed of the physical model of the marine fluidized bed boiler. *J Pol CIMAC.* 2008;3(1):183–190.
33. Schubert M, Khetan A, Da Silva MJ, Kryk H. Spatially resolved inline measurement of liquid velocity in TBRs. *Chem Eng J.* 2010;158(3):623–632.
34. Kan K-M, Greenfield PF. Multiple hydrodynamic states in concurrent two phase down flow through packed beds. *Ind Eng Chem Process Des Dev.* 1978;17:482–485.
35. Boelhouwer JG, Piepers HW, Drinkenburg AAH. Nature and characteristics of pulsing flow in trickle-bed reactors. *Chem Eng Sci.* 2002;57(22–23):4865–4876.
36. Moskowitz J. Estimates of the power spectrums for fully developed seas for wind speeds of 20 to 40 knots. *J Geophys Res.* 1964;69(24):5161–5179.
37. Da Silva MJ, Schleicher E, Hampel U. Capacitance wire-mesh sensor for fast measurement of phase fraction distribution. *Meas Sci Technol.* 2007;18(7):2245–2251.
38. Schleicher et al. Refined reconstruction of liquid-gas interface structures for oil-gas stratified two-phase flow using wire-mesh sensor. In: *5th International Workshop on Process Tomography*, Jeju, South Korea, 2014.
39. Hamidipour M, Larachi F. Modulation of suspension electrical conductivity to counter fines plugging in trickle-bed reactors. *AIChE J.* 2011;57(7):1829–1839.
40. Aydın B, Larachi F. TBR hydrodynamics and flow regime transition at elevated temperature for a Newtonian and a non-Newtonian liquid. *Chem Eng Sci.* 2005;60(23):6687–6701.
41. Hamidipour M, Larachi F, Ring Z. Monitoring filtration in TBRs using electrical capacitance tomography. *Ind Eng Chem Res.* 2009;48(3):1140–1153.
42. Llamas J-D, Lesage F, Wild G. Influence of gas flow rate on liquid distribution in trickle-beds using perforated plates as liquid distributors. *Ind Eng Chem Res.* 2009;48(1):7–11.
43. Wakao N, Kaguei S. *Heat and Mass Transfer in Packed Beds*. New York: Gordon and Breach Science Publishers, 1982.
44. Levenspiel O. *Chemical Reaction Engineering*, 3rd ed. New York: Wiley, 1999.

*Manuscript received Nov. 5, 2014, and revision received Feb. 26, 2015.*